AJNR

Neuroimaging in Pediatric Brain Tumors: Gd-DTPA–enhanced, Hemodynamic, and Diffusion MR Imaging Compared with MR Spectroscopic Imaging

A. Aria Tzika, Maria K. Zarifi, Liliana Goumnerova, Loukas G. Astrakas, David Zurakowski, Tina Young-Poussaint, Douglas C. Anthony, R. Michael Scott and Peter McL. Black

AJNR Am J Neuroradiol 2002, 23 (2) 322-333
http://www.ajnr.org/content/23/2/322

AJNR Am J Neuroradiol 23:322–333, February 2002

Neuroimaging in Pediatric Brain Tumors: Gd-DTPA–enhanced, Hemodynamic, and Diffusion MR Imaging Compared with MR Spectroscopic Imaging

A. Aria Tzika, Maria K. Zarifi, Liliana Goumnerova, Loukas G. Astrakas, David Zurakowski, Tina Young-Poussaint, Douglas C. Anthony, R. Michael Scott, and Peter McL. Black

BACKGROUND AND PURPOSE: **Gadolinium-enhanced MR images assist in defining tumor borders; however, the relation between tumor cell extent and contrast-enhanced regions is unclear. Our aim was to improve conventional neuroimaging of pediatric brain tumors with hemodynamic, diffusion, and spectroscopic MR imaging.**

METHODS: **We performed conventional MR and MR spectroscopic imaging in 31 children with neuroglial brain tumors. Hemodynamic MR imaging was performed in 16 patients with a first-pass intravenous bolus of gadolinium diethylenetriaminepentaacetic acid (Gd-DTPA); apparent diffusion coefficients (ADCs) were measured in 12 patients. To account for multiple measurements in a patient, we used a nested analysis of variance.**

RESULTS: **At MR spectroscopy, choline (Cho)-containing compounds (indicating tumor) and lipid levels (indicating necrosis) did not correlate with percent Gd-DTPA enhancement on MR images. Percent enhancement was positively correlated with relative cerebral blood volumes (rCBVs) ($P = .05$) and negatively correlated with ADCs ($P < .001$). Stepwise multiple linear regression revealed that rCBV ($P = .008$), ADC ($P = .022$), and lipid ($P < .001$) levels were significant independent predictors of percent enhancement. Tumor spectral patterns were detected in tumor regions and outside enhancing tumor beds in patients with clinical progression; these were confirmed at neuropathologic analysis.**

CONCLUSION: **MR spectroscopic imaging improves the assessment of pediatric brain tumors by adding biochemical information regarding tumor involvement and by depicting residual or recurrent tumor outside the Gd-DTPA–enhanced tumor bed. rCBV and ADC mapping complemented MR spectroscopic imaging. We recommend the use of MR spectroscopic imaging in addition to conventional MR imaging in assessing pediatric brain tumors.**

MR imaging is widely used in the diagnosis and follow-up of pediatric patients with brain tumors because of its ability to provide anatomic detail. However, conventional MR imaging does not provide information about tissue biochemistry. In addition, it has shortcomings in the classification of tumors or degree of malignancy. Finally, interpretation of conventional MR images may lead to poor estimation of the extent of active tumor. MR contrast enhancement assists in defining tumor borders, but it is not reliable in the determination of malignancy (1). Histologic examination can be used to identify tumor cells that extend beyond the tumor border, as depicted on T2-weighted MR images (2). On the other hand, false-positive MR contrast enhancement in recurrent lesions has been reported (3), and postradiation necrosis may mimic tumor on MR images (4). Thus, MR imaging frequently cannot be used to identify an entire tumor and to differentiate between therapy-related tissue reactions and the progression or recurrence of tumors. Therefore, the identification of patients who are likely to benefit from aggressive treatment strategies relies on stereotactic biopsy be-

Received April 5, 2001; accepted after revision September 26.

From the Departments of Radiology (A.A.T., M.K.Z., L.G.A., T.Y.-P.), Neurosurgery (L.G., R.M.S., P.McL.B.), Pathology (D.C.A.), and Biostatistics (D.Z.), Children's Hospital, Harvard Medical School, Boston, MA.

Supported by American Cancer Society grant RPG-98–056-01-CCE.

Address reprint requests to A. Aria Tzika, PhD, Director of the NMR Surgical Laboratory, Massachusetts General Hospital, Harvard Medical School and Shriners Burns Institute, 51 Blossom Street, Room 261, Boston, MA 02114.

cause a noninvasive method such as MR imaging is frequently limited.

Gadolinium diethylenetriaminepentaacetic acid (Gd-DTPA) is a clinically used MR contrast agent. Intravenous administration of Gd-DTPA may result in enhancement on T1-weighted MR images of certain brain tumors because of a breakdown in the blood-brain barrier. Whether necrotic tumors enhance and whether necrosis is hypointense remains unclear. However, enhancement has been used to indicate tumor aggressiveness and recurrence and the extent of active tumor.

Recent studies have shown that proton MR spectroscopic imaging can depict substantial differences between the in vivo spectra of three tissue compartments: tumor, necrosis, and healthy brain (5, 6). Additional characterization of these compartments can be obtained with hemodynamic MR imaging and diffusion-weighted MR imaging. Parameters derived from MR spectroscopic imaging include those involving *N*-acetylaspartate (NAA), choline (Cho)-containing compounds, total creatine (tCr), and lipids. Parameters obtained from hemodynamic and diffusion-weighted MR imaging include the relative cerebral blood volume (rCBV) and apparent diffusion coefficient (ADC), respectively.

The aim of this study was to improve conventional neuroimaging of pediatric brain tumors by adding biochemical information obtained with MR spectroscopic imaging, hemodynamic data obtained with rCBV mapping, and physical chemical information obtained with ADC mapping. Our hypothesis was that biochemical parameters, as detected with MR spectroscopic imaging, contribute independent nonrepetitive information beyond that obtained with MR imaging. This information may be helpful in the assessment of pediatric brain tumors.

Methods

Patients

Thirty-one patients with neuroglial tumors underwent conventional MR imaging and MR spectroscopic imaging; 16 patients underwent hemodynamic MR imaging, and 12 of the 16 underwent diffusion-weighted MR imaging. The mean age of the patients was 10 years (range, 6 months to 16 years). When necessary, sedatives (midazolam hydrochloride 0.1 mg/kg, lorazepam 0.1 mg/kg, or chloral hydrate 50 mg/kg by mouth) were administered to the patients. Children were examined at initial presentation or immediately after surgery and before any adjuvant treatment (radiation therapy or chemotherapy or both). Follow-up conventional and spectroscopic MR images and hemodynamic MR images were included in this study; diffusion-weighted images obtained in four children with malignant recurrent tumors were not included. Recurrence was verified with stereotactic biopsy, as well as the clinical course. We included only follow-up MR images obtained after the acute phase of radiation (approximately 3 months) to ensure that nonspecific posttreatment effects did not affect our observations.

The pathologic classification used in our institution is the World Health Organization classification of brain tumors (7, 8). The two main categories of tumors included in this study were glial tumors and embryonal neuroglial tumors. Tumors were classified at biopsy as follows: pilocytic astrocytomas (n = 6), grade I astrocytomas (n = 2), ependymomas (n = 3), poorly differentiated (embryonal) tumors (n = 4), medulloblastomas (n = 2), pineoblastomas (n = 2), anaplastic astrocytomas (n = 2), choroid plexus carcinomas (n = 2), and gangliogliomas (n = 2). Pilocytic astrocytomas, grade I astrocytomas, and gangliogliomas were classified as benign tumors, whereas ependymomas, medulloblastomas, pineoblastomas, anaplastic astrocytomas, choroid plexus carcinomas, and other embryonal tumors were classified as malignant tumors. Therefore, we examined 10 patients with benign tumors and 15 with malignant tumors. The remaining six patients with inoperable glial tumors (eg, brain stem gliomas) did not have a histopathologic diagnosis. Informed consent was obtained from each participant's parent or guardian before his or her inclusion in the study if the study was not clinically indicated.

To spatially correlate the histopathologic information to the MR data, we obtained biopsy samples with the guidance of a surgical navigation system to determine the location of each biopsy site on the MR images. Thus, immediately before the removal of a biopsy specimen, a multiplanar MR image of the origin of the sample was saved by using an ISG Viewing Wand (ISG Technologies, Missisauga, Ontario, Canada). Each sample was then obtained with small surgical forceps, labeled, handled separately, and submitted for routine pathologic examination.

MR Methods

MR examinations were performed with a 1.5-T, whole-body imaging and spectroscopic MR system (GE Medical Systems, Milwaukee, WI) and a quadrature head coil. Our system permitted conventional imaging, as well as echo-planar and multilevel hemodynamic MR imaging. In addition, we used our automated spectroscopic acquisition routines, which resulted in faster data acquisition (approximately 4 minutes per 2D spectroscopic data set with $1 \times 1 \times 1$-cm resolution). These acquisitions were possible at adjacent levels (no gap). Hemodynamic and diffusion-weighted MR images were acquired at corresponding levels. Multilevel 2D MR data acquisitions with no gap were used rather than 3D methods. This approach improved the signal-to-noise ratio, because adjustments for magnetic field homogeneity and water suppression were performed in each section; with a large volume, these adjustments often fail in the clinical MR setting. The levels of hemodynamic, diffusion, and spectroscopic MR images were chosen after the conventional T1-weighted, T2-weighted, and fluid-attenuated inversion recovery (FLAIR) images were evaluated to include the tumor and surrounding tissues.

Pediatric neurologists (M.K.Z., T.Y.-P.) who were blinded to the findings of MR spectroscopy and perfusion and diffusion imaging studied the MR images. These images were then compared with the multivoxel data obtained at proton MR spectroscopy, as well as with the perfusion and diffusion images at the appropriate level. In as much as our multivoxel data included the tumor (as defined on conventional MR images) and surroundings, we avoided interjecting a bias and assumed that Gd enhancement could be used to identify the extent of the tumor. Thus, we were able to test the hypothesis that MR spectroscopy depicts tumor outside the Gd-enhancing tumor bed.

Hemodynamic and diffusion-weighted MR imaging were performed by using echo-planar and line-scan techniques, respectively (9, 10). Hemodynamic images (rCBV maps) and calculated diffusion images (ADC maps) were generated on a remote workstation (Sun Microsystems, Mountain View, CA). Hemodynamic MR imaging was performed by using a single-shot echo-planar T2*-weighted method during a compact bolus injection of Gd-DTPA, with a 1.5-T MR system (9). A clinical dose (0.1 mmol/kg, 0.2 mL/kg) of gadolinium-based contrast agent was administered intravenously by using an automatic injector with a power injector rate of 1–2 mL/s. To ensure the quality of the hemodynamic MR images, the intravenous line

was placed before the patient entered the MR unit. Twenty-five images were acquired in nine adjacent axial sections (10 mm thick) within 1.25 minutes. Typical parameters for hemodynamic MR imaging were 300/40/1 (TR/TE/NEX), with a FOV of 40 cm.

The diffusion-weighted MR imaging method used in our study has been described previously (10). Briefly, diffusion-weighted imaging was performed by using a line-scan method to acquire axial images (FOV, 20 × 15 cm; effective section thickness, 7 mm; gap, 0 mm; acquisition matrix, 128 × 128 interpolated to 256 × 192; b = 5 and 750 s/mm^2 as the maximum b value applied along the three orthogonal directions). The minimum imaging time was 5 minutes 49 seconds. ADC maps and trace images extrapolated to a b value of 1000 s/mm^2 were generated offline for each of the 10 locations. The trace images were calculated as the cubed root of the product of the three diffusion axes.

Proton MR spectroscopic imaging was performed by using multivoxel chemical shift imaging with point-resolved spectroscopy (PRESS) and volume preselection (5). Briefly, after a 50–100-mL volume was selected and after shimming and water suppression adjustments were made, a large data set was obtained by using phase-encoding gradients in two directions. The following parameters were used: 1000/65 (TR/TE), 16 × 16 phase-encoding matrix, 160-mm FOV, section thickness of 10 mm, 1250-Hz spectral width, two averages, and 512 points. Data sets of 1–1.2-cm^3 resolution were acquired. The decision to use a TE of 65 milliseconds was made for the following reasons. In our study, we were not as interested in the lactic acid detection as in the presence of lipids, which might be important, because lipids are related to tumor necrosis or apoptosis; this, in turn, is a determining factor of tumor activity. Our pretest hypothesis was that a TE of 65 milliseconds provides us with the opportunity to 1) null lactic acid; 2) increase sensitivity in lipid detection, and 3) prevent diffusion artifacts and water-suppression failures with PRESS performed at TEs shorter than 65 milliseconds. Thus, the four prominent peaks of biologic importance in our studies were those of NAA, Cho, tCr, and lipids (and/or lactate). Data were processed on a workstation (Sun Microsystems) by using analysis software (SAGE; GE Medical Systems) and software developed in-house by using interactive data language (IDL) 5.3 (Research Systems, Boulder, CO). The data sets were apodized with a 1.0-Hz lorentzian filter, Fourier transformed in the time domain and two spatial domains, and phased (first automatically and then manually if necessary) by using the SAGE spectroscopic analysis software (GE Medical Systems) . Then, a baseline estimator was used to subtract the broad components of the baseline before peak area calculations. Finally, the areas of selected metabolite peaks were estimated by using the PIQABLE algorithm developed in IDL. Metabolite images were generated and stored as tiff files on a SPARC workstation (Sun Microsystems) and then transferred to a Macintosh workstation (Apple Computer, Cupertino, CA). We used imaging editing software such as NIH Image (National Institutes of Health, Bethesda, MD) and Photoshop (Adobe, San Jose, CA) to overlay the metabolite images on the corresponding anatomic images.

Normalized MR spectroscopy–derived parameters (Cho, lipids) were compared with rCBV and ADC values. We normalized these parameters by dividing their values from within tumor regions by the mean value of tCr in normal tissue in each patient, which can be used as a reasonable internal standard (11). Thus, our spectroscopy-derived parameters were expressed in arbitrary units. We also normalized values in the same tumor regions of interest on rCBV maps with values obtained from within the middle cerebral artery territory in the same patient. The rCBV values were also expressed in arbitrary units. ADC values were expressed as a number × 10^{-2} in units of square millimeter per millisecond. Percent enhancement in the tumors was calculated by subtracting the enhancement within normal tissue from the enhancement within tumor tissue and by dividing this by the enhancement within normal tissue and multiplying the result by 100. Multiple measurements were obtained in each patient to account for brain tumor heterogeneity.

Biostatistical Analysis

Results of the Kolmogorov-Smirnov test of normality indicated that Cho, rCBV, ADC, and percent enhancement values did not significantly depart from a gaussian distribution. Therefore, the Pearson product-moment correlation coefficient, r, and a linear regression analysis were used to evaluate the strength of relationships. Stepwise multiple linear regression was performed to identify independent predictors of percent enhancement. Because the data for lipids were heavily skewed and because they did not conform to a normal distribution, a natural logarithmic transformation was used to normalize the lipid variable. For correlational analysis, the number of measurements included 139 for percent enhancement, Cho, and lipids; 68 for rCBV; and 48 for ADC. To account for the multiple measurements within the same patient, we also used a nested analysis of variance approach to test the relationship among the variables (12). SAS statistical software (version 6.12; SAS Institute, Cary, NC) was used to analyze the data. All reported *P* values are two tailed, and *P* values of less than .05 were considered to indicate statistically significant differences.

Results

Figure 1 illustrates the relationship between percent enhancement and Cho, lipids, rCBV, and ADC values. The data for selected patients are shown in Figures 2–6. Although MR spectral patterns were different in healthy areas (all three Cho, tCr, and NAA peaks), tumor (prominent Cho), and necrotic regions (lipids or no metabolite peaks), mixed MR spectral patterns (ie, spectra 3 and 4 in Fig 2) were also shown (Figs 2–6). At histopathologic analysis, for which data in 25 patients (15 with malignant and 10 with benign tumors) were available, mixed spectral patterns within the enhancing tumor bed were verified as regions of both tumor and necrosis (spectrum 3 in Fig 2), which occasionally included some neurons (spectrum 4 in Fig 2).

Analysis of 139 measurements in 31 patients revealed that percent Gd-DTPA enhancement did not correlate with normalized Cho (r = 0.14, $P = .10$) (Fig 1A) or lipid levels (r = 0.08, $P = .36$) (Fig 1B). Meanwhile, significant positive and inverse correlations existed between percent enhancement and rCBV in 16 patients with 68 measurements (r = 0.28, $P = .05$) (Fig 1C) and between percent enhancement and ADC in 12 patients with 48 measurements (r = −0.57, $P < .001$) (Fig 1D). Stepwise multiple linear regression revealed that rCBV ($P = .008$), ADC ($P = .022$) and lipid values ($P < .001$) were significant independent predictors of percent enhancement. Cho was not a significant predictor of percent enhancement ($P = 0.70$) in the multivariate model.

In addition, Cho was not only detected in regions of contrast enhancement but also in areas outside the Gd-DTPA–enhanced tumor bed, which eventually

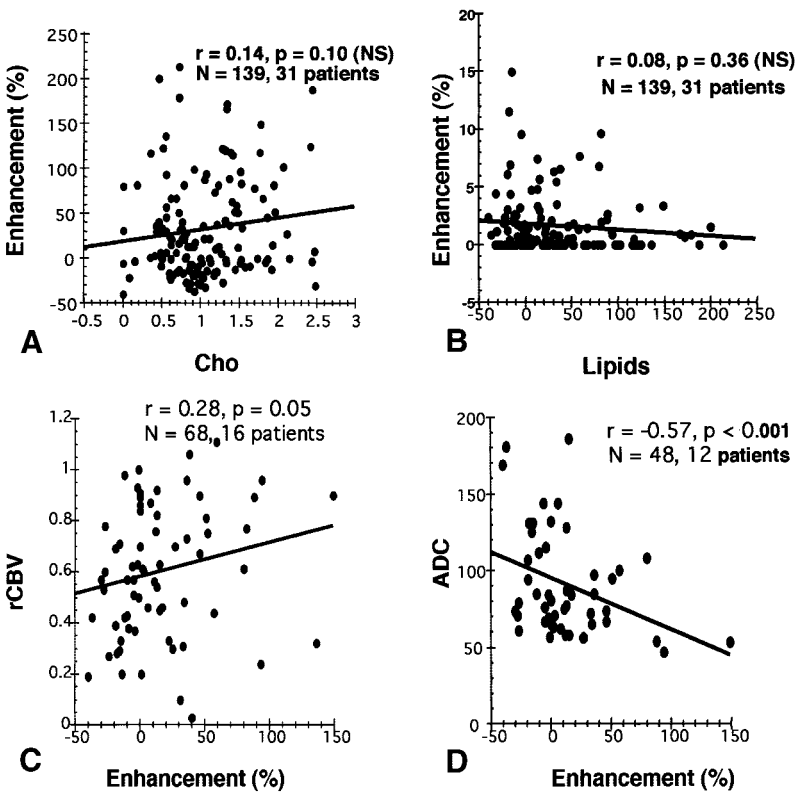

FIG 1. Plots show the relationships between percent enhancement and Cho (*A*), lipids (*B*), rCBV (*C*), and ADC (*D*). The number of measurements (*N*) and the number of patients are shown. The fitted regression line, Pearson correlation *r*, and *P* values are also shown.

enhanced on follow-up images (Figs 2, 4–6), and within the tumor itself, as depicted on T2-weighted images, when the tumor did not enhance (Fig 3). MR spectroscopic imaging revealed at least one spectrum with high Cho levels in nonenhancing regions that were neighboring or outside the Gd-DTPA–enhanced tumor bed in 15 patients with malignant tumors—that is, patients with choroid plexus carcinoma (Fig 2), anaplastic astrocytoma (Figs 5, 6), ependymoma, poorly differentiated tumors, and medulloblastoma—and in three patients with inoperable tumors (no such areas were identified in patients with benign tumors). The sites outside the Gd-DTPA–enhanced tumor bed (suggestive of tumor involvement on MR spectroscopic images) were the sites for recurrence in four patients in whom subsequent tumor recurrence was diagnosed during the course of the study. Recurrence was verified not only with the clinical course but also with neuropathologic findings obtained after repeat operations or stereotactic biopsy during the course of the study. The MR spectroscopic imaging findings from two examinations in one patient are illustrated in Figures 5 and 6.

We also found that, in the 15 patients with malignant tumors and three patients with inoperable tumors, contrast-enhancing regions did not always have high Cho levels. At least one spectrum with a very low or no Cho level and a high lipid (and/or lactate) level was identified in 11 of these patients. Such spectra were assumed to correspond to regions of high neoplastic potential intermingled with microscopic necrosis (Fig 4). Such areas were identified by means of neuropathologic analysis of stereotactic biopsy samples in four patients; they were found to correspond to MR spectra with low Cho and high lipids values (Figs 5, 6). In the 10 patients with benign tumors, no such areas were noted.

Furthermore, we found that nonenhancing regions in certain tumors were dominated by prominent lipid and less prominent Cho signals. This is illustrated in region 5 in Figure 2, the posterior aspect of the tumor in Figure 4, and in Figures 5 and 6. These were presumed to represent necrotic or cystic and/or necrotic areas, as verified at neuropathologic examination in the 15 patients with operable malignant tumors. Necrotic areas with low Cho levels were occasionally present in patients with benign tumors.

Finally, Gd-DTPA enhancement coincided with bright regions on hemodynamic images, as illustrated in Figures 2 and 4. However, rCBV maps did not show abnormal rCBV outside the Gd-DTPA–enhanced tumor bed, as illustrated in Figure 2. However, in the four patients who underwent follow-up evaluation, high rCBV values corresponded to the ring of enhancement and regions of high Cho levels outside the Gd-DTPA–enhanced tumor bed, as illustrated by the hyperintense regions 3 and 4 of the rCBV map in Figure 6. ADC maps were not available in these four patients with follow-up findings.

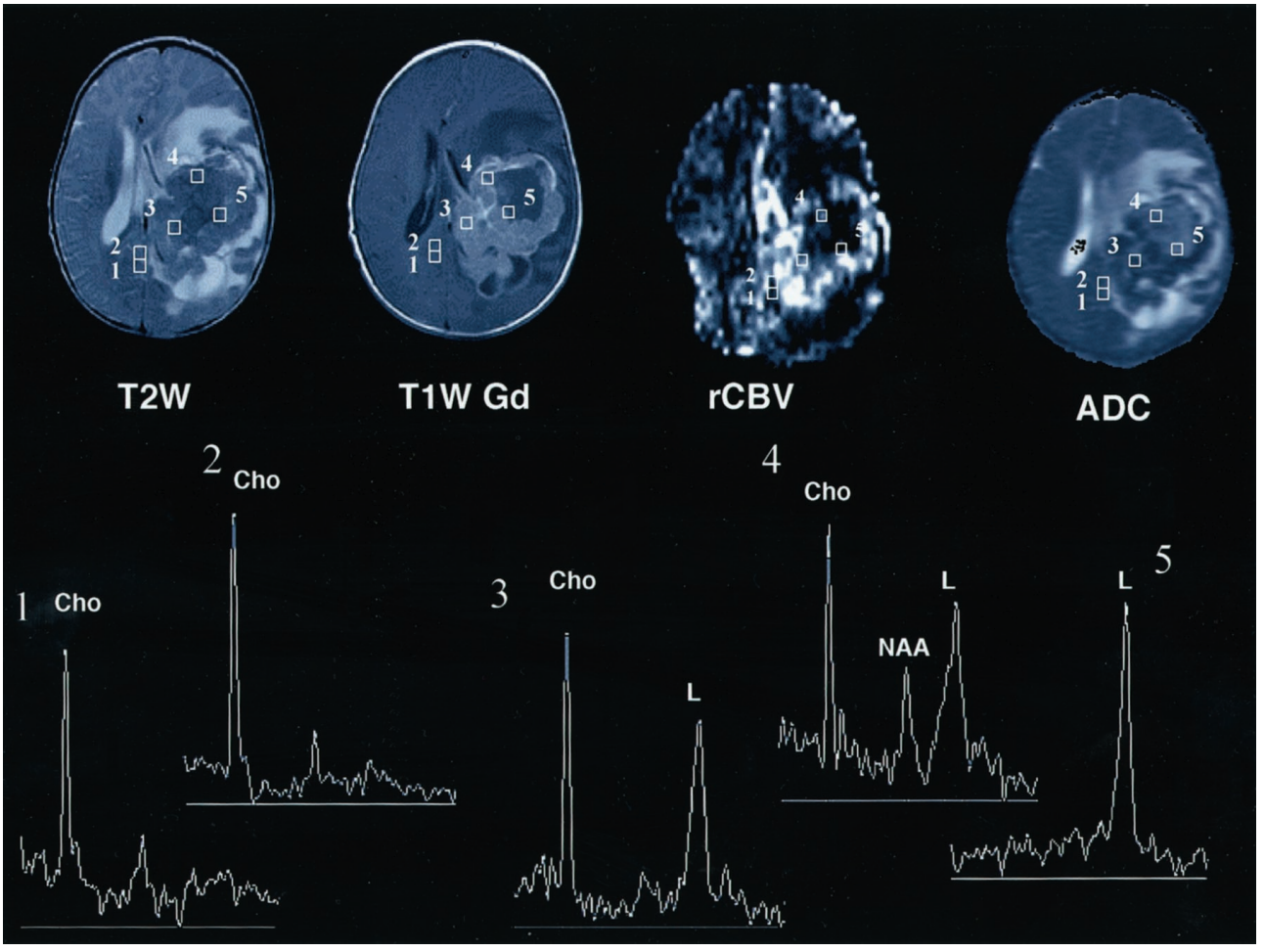

FIG 2. Axial T2-weighted (*T2W*), T1-weighted Gd-enhanced (*T1W Gd*), hemodynamic (*rCBV*), and diffusion (*ADC*) MR images and selected proton MR spectra (*1–5*) from a multivoxel spectroscopic data set in a 6-month-old male infant with a choroid plexus carcinoma. The lesion contains a large central area of low or normal signal intensity on the T2-weighted image, and it has inhomogeneous intense enhancement on the T1-weighted Gd-enhanced image, with nonenhancing areas that represent necrotic and/or cystic degeneration. The rCBV image shows increased perfusion (bright regions) in the areas of enhancement, whereas the corresponding areas on the ADC image appear hypointense. Selected proton MR spectra (*1–4*) show high Cho peaks, which are believed to correspond to areas of viable tumor. MR spectra *1* and *2* correspond to areas of low or normal signal intensity on the T2-weighted image that do not enhance on the T1-weighted; theses areas appear hypointense on both rCBV and ADC images. MR spectra *3* and *4* correspond to hypointense areas on the T2-weighted image that enhance; these appear hyperintense and hypointense on rCBV and ADC images. MR spectrum *5* shows only a high lipid (*L*) value, which is thought to indicate necrosis; this finding corresponds to a hypointense region on the T2-weighted image that does not enhance on the T1-weighted Gd-enhanced and rCBV images and appears hyperintense on the ADC image. High lipid values are also shown on MR spectra *3* and *4*, in addition to high Cho values; this pattern indicates a mixture of viable tumor and necrosis. The Figure illustrates a positive relationship between Cho and rCBV values and an inverse relationship between Cho and ADC values. It shows that Cho (or active tumor) was detected in enhancing regions of the tumor and beyond.

Discussion

Our hypothesis was that biochemical parameters, as detected with MR spectroscopic imaging, contribute independent nonrepetitive information beyond that obtained with conventional MR imaging in pediatric brain tumors; with MR imaging, the location and size seem to be better predictors of malignancy than specific imaging characteristics (1). Our results verified our hypothesis to the extent anticipated, because we showed that no relationship exists between Gd-DTPA enhancement and other MR spectroscopic parameters. Also, tumor spectral patterns were detected outside the Gd-DTPA–enhanced tumor bed in malignant tumors. In summary, Gd-DTPA enhancement at conventional MR imaging did not correlate with either Cho or lipid findings obtained at MR spectroscopic imaging, although it did correlate with rCBV and ADC results.

Choline-Containing Compounds

In our study, Gd-DTPA enhancement on conventional MR images did not correlate with Cho findings (Fig 1A). Meanwhile, Sijens et al (13, 14) reported that, for large lesions (with a single-voxel proton MR spectroscopic method in 15 patients), Cho findings were significantly correlated with percent tumor enhancement. The lack of agreement between our findings and those of Sijens et al may be due to different tumor histologic features, because they examined

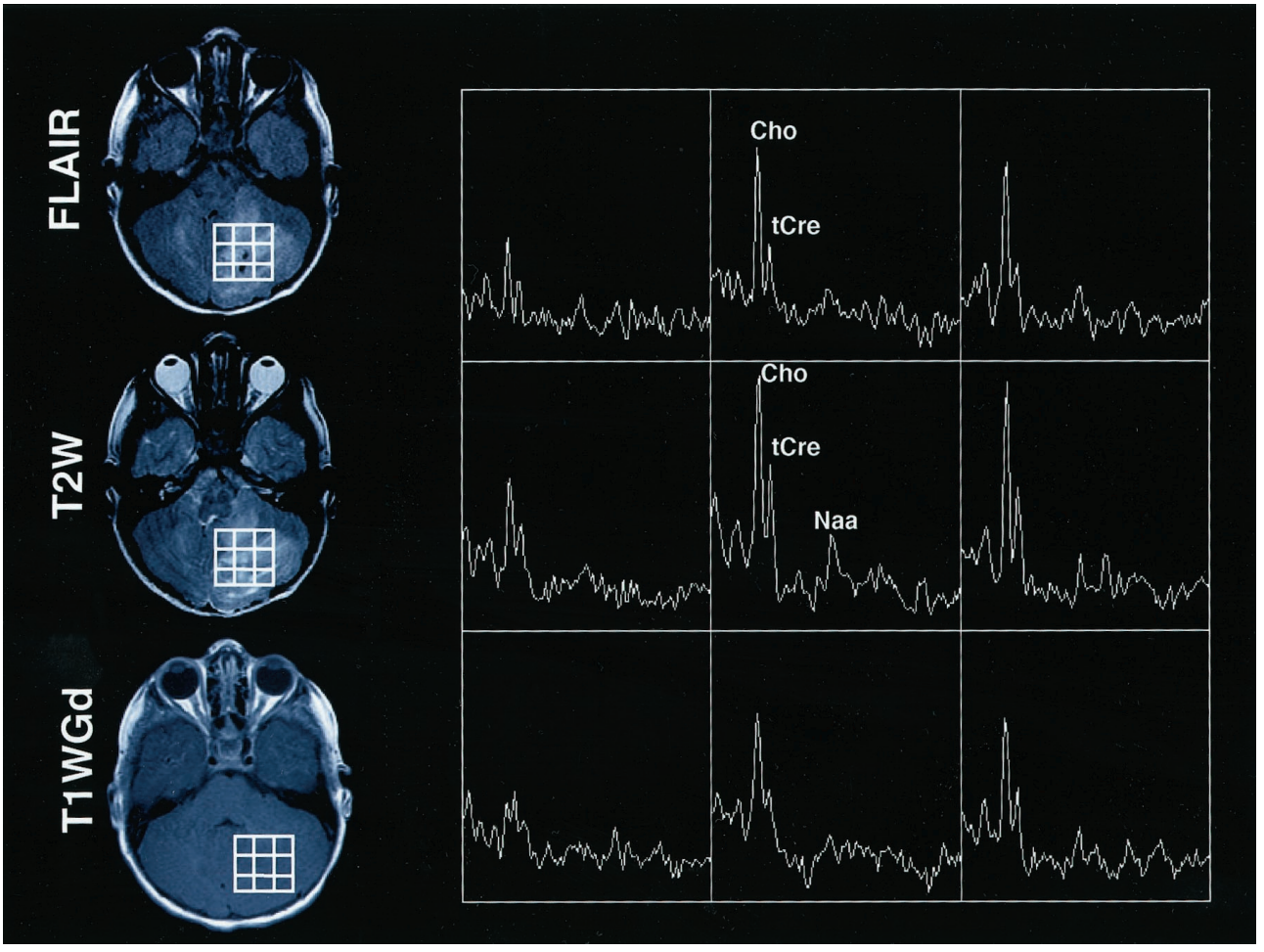

FIG 3. Axial FLAIR, T2-weighted (*T2W*), and T1-weighted Gd-enhanced (*T1WGd*) MR images and selected proton MR spectra from a multivoxel MR spectroscopic data set in a 10-year-old girl with a cerebellar tumor. The lesion appears inhomogeneously hyperintense on the FLAIR and T2-weighted images and is not enhancing on the T1-weighted Gd-enhanced image. Prominent peaks corresponding to Cho are detected. Also, tCr and NAA peaks are occasionally detected. The Figure illustrates that no relationship existed between Cho detection and contrast enhancement on T1-weighted Gd-enhanced images.

adult patients with brain metastasis of breast carcinoma. Also, their single-voxel approach and their analysis, which included regions of necrosis, led to the interpretation that their correlation was due to a decrease in cellularity and Gd-DTPA delivery to necrotic areas (14). We studied pediatric brain tumors, which are known to have histopathologic characteristics that differ from those of adult tumors. Also, we used a multivoxel method with $1 \times 1 \times 1$-cm resolution, which better addressed tumor heterogeneity, instead of a single-voxel approach in which viable tumor and necrosis are averaged over a volume of interest that is typically much larger than 1 cm^3. Viable tumor growth and necrosis have different spectral patterns (5, 6).

Elevated Cho levels were detected in both enhancing (Fig 2) and nonenhancing (Fig 3) tumors. Published reports of proton MR spectra in adults (6, 11, 15) and children (5, 16–18) with untreated brain tumors and in brain metastases have also indicated high levels of Cho. Although compounds contributing to the Cho signal in vivo have been suggested (19), the particular compound that increases with neoplasia remains essentially unknown. Moreover, Cho has been associated with increased cellularity (17, 20–22), membrane synthesis, and rapid cell turnover or proliferative activity (15, 23, 24). Cho was proposed to be the most reliable indicator of malignancy in gliomas (15); also, it has been shown to increase with benign brain tumors in children (17, 25).

Our patients who underwent follow-up MR examination had elevated Cho levels and recurrence before the appearance of contrast-enhancing regions on conventional MR images (Figs 5 and 6). In other studies (6, 15, 26), highly elevated Cho levels on the posttreatment proton MR spectra were thought to indicate areas of recurrence or progressive disease or malignant transformation or both rather than areas of radiation necrosis. On the other hand, increases in Cho levels have been observed both in animals and after irradiation of normal brain tissue (27) and in patients with brain tumor shortly after radiation treatment (28). They have been attributed to the breakdown of membrane lipids with an elevation in the level of water-soluble mobile phosphocholine (29) and with demyelination of the brain caused by the

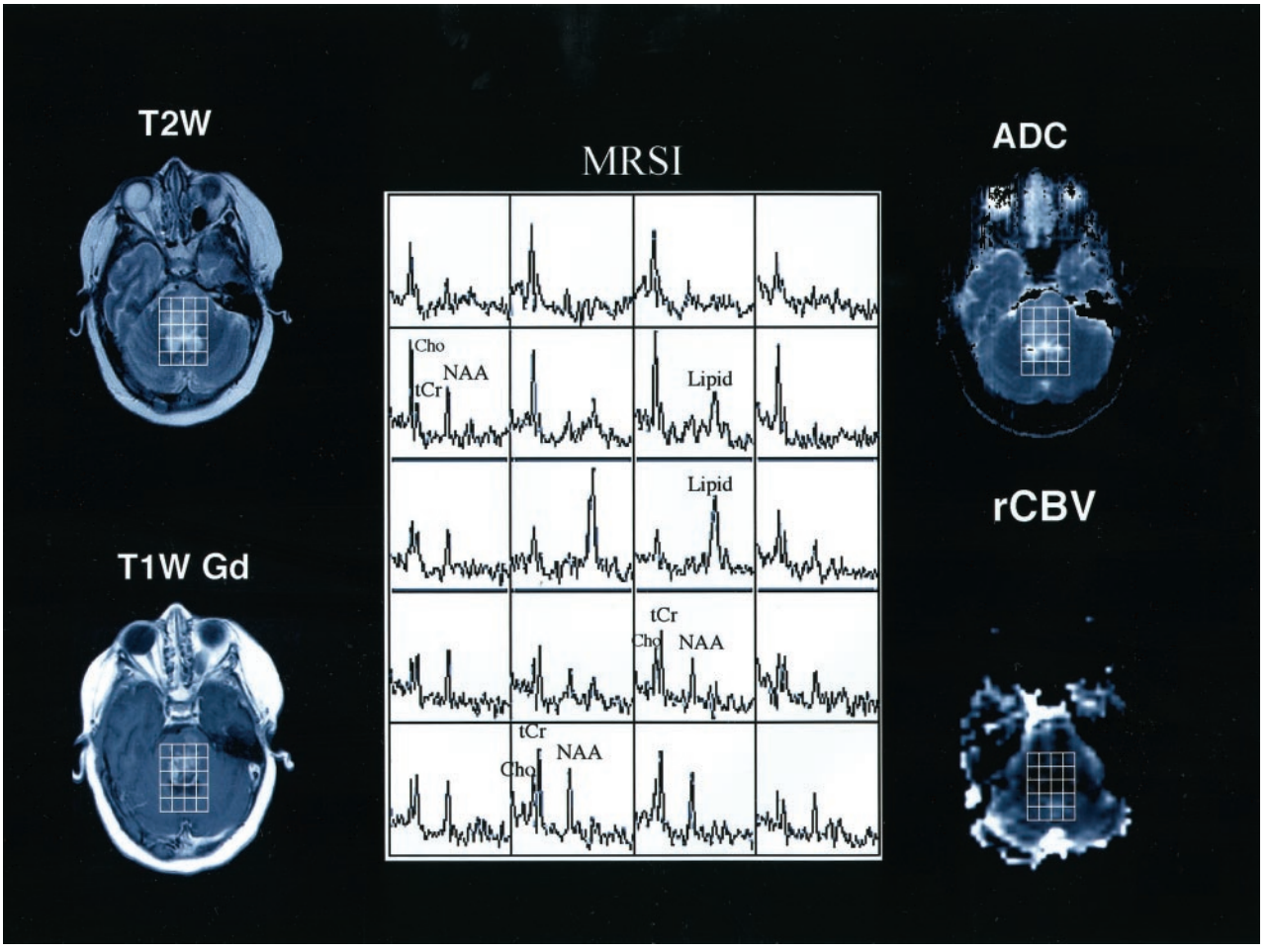

FIG 4. Axial T2-weighted (*T2W*), T1-weighted Gd-enhanced (*T1W Gd*), hemodynamic (*rCBV*), diffusion (*ADC*) MR images and selected proton MR spectra (*MRSI*) from a multivoxel MR spectroscopic data set in a 16-year-old male adolescent with an enlarging inoperable brainstem lesion that was identified after the acute onset of left-sided nerve palsy. The lesion with high signal intensity on the T2-weighted image appears hyperintense on the T1-weighted Gd-enhanced and ADC images, and it is hypointense on the rCBV image. Multivoxel proton MR spectra (TE, 65 milliseconds) show a large lipid peak, in addition to Cho and tCr peaks, within the central portion of the mass; in the anterior voxel, the same peak was absent. These findings suggest that the lesion has a high neoplastic potential because increased lipid levels represent necrosis. Findings on both rCBV and ADC images are not consistent with the MR spectroscopic findings.

destruction of oligodendrocytes and/or myelin with the subsequent release of Cho (30, 31). Nevertheless, in our study, we included the patients with follow-up MR findings obtained only after the acute phase of radiation (approximately 3 months) to ensure that nonspecific postradiation effects did not affect our observations about Cho.

Our finding that no correlation existed between Cho values and percent tumor enhancement and that regions with high Cho levels existed beyond the contrast-enhancing regions (Figs 2–4) agree with those of other investigators who studied adult glioblastoma multiforme (6). Therefore, we believe that percent enhancement, although it coincides with blood-brain barrier breakdown, does not necessarily indicate an early phase of tumor growth, which seems to be better detected with proton MR spectroscopy. We also believe that Cho mapping adds value to conventional MR imaging, especially if it is combined with lipid mapping.

Lipids

In our study, peaks at 1.33 ppm, which we identified as lipid peaks, were not detected in all patients. We considered that these peaks primarily consisted of lipids and secondarily lactate, because our acquisition protocol, with a TE of 65 milliseconds, was not optimized to depict lactate. Some colleagues (32–34) have focused on lactate and tailored their protocols accordingly; they showed that lactate is an indicator of tumor metabolic activity, while others have disputed the role of lactate as an indicator of malignancy (35, 36). Thus, the role of lactate at in vivo MR spectroscopy of tumors cannot be established until the appropriate pulse sequences and protocols for lactate detection are implemented in the clinical setting (36–38). In our study, a TE of 65 milliseconds was chosen because this was the shortest TE that could be implemented to achieve T2 weighting and sensitivity to detect metabolites with short TEs, such as lipids. Peaks at the 0.8–1.8-ppm range are probably due to

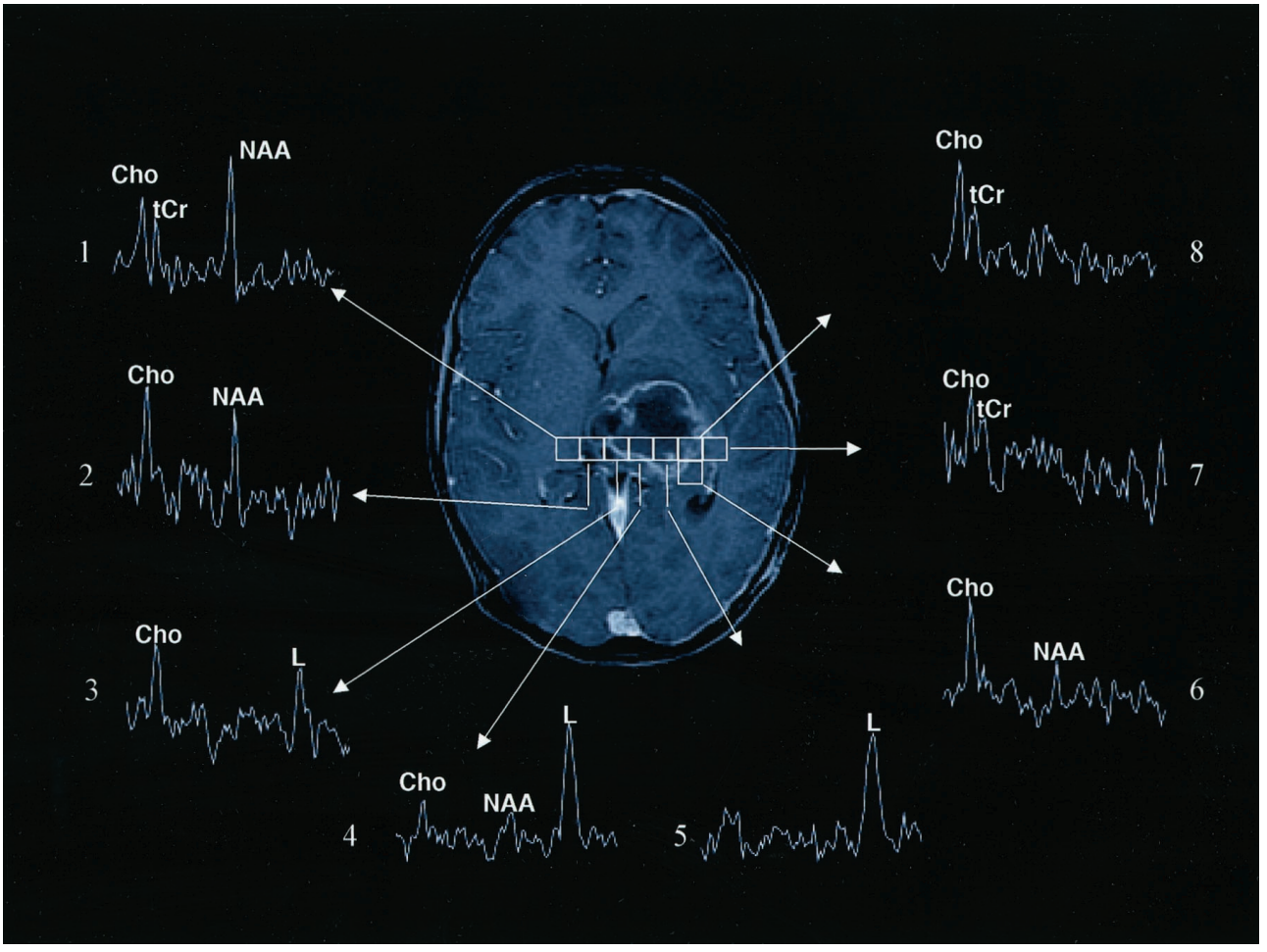

FIG 5. Images obtained at the first follow-up evaluation (after radiation therapy and chemotherapy) include an axial T1-weighted Gd-enhanced MR image and multivoxel MR spectra in a male patient with an anaplastic (malignant) astrocytoma in the left thalamus. Selected proton MR spectra (*1–8*) illustrate that tumor spectral patterns were detected beyond the contrast-enhancing region and that regions of tumor corresponded to necrotic spectral patterns. Spectrum *1* shows a pattern that is characteristic of normal tissue, because all three biologically important metabolites (NAA, Cho, tCr) are detected. The voxel corresponding to spectrum *2* includes enhancing tissue and shows increased Cho and prominent NAA levels; this spectral pattern is characteristic of mixed tumor and normal tissue. Spectrum *3* shows a spectral pattern with only Cho and lipids (*L*) values; this is consistent with tumor and necrosis and corresponds to both enhancing and nonenhancing tissue. Spectrum *4* shows extensive necrosis (prominent lipids), along with some normal and tumor tissue (Cho and NAA peaks). Spectrum *5* shows primarily necrosis (predominantly lipid) and, possibly, some tumor. Voxels corresponding to spectra *6* and *7* show minimal enhancement, whereas the voxel that corresponds to spectrum *8* includes areas of enhancement. Spectra *6–8* show tumor spectral patterns (prominent Cho and tCr) and correspond to regions of contrast enhancement (spectrum *8*) and beyond (spectra *6* and *7*).

aliphatic compounds (lipids) and other macromolecules (proteins). Recently, certain investigators (21, 39–42) have increasingly considered lipids to be important indicators of tumor cellular activity and indices of tumor grade. Our data are consistent with this notion, and this observation may be of biologic importance, since lipid levels also substantially increased in active tumors versus inactive tumors (43).

In our study, the presence of lipids in tumors, as detected at MR spectroscopic imaging, was not correlated with Gd-DTPA enhancement at conventional MR imaging (Fig 1B). Prominent lipids were detected in both enhancing and nonenhancing parts of tumors (Fig 2). This result was in agreement with the notion that lipids represent microscopic tumor cell necrosis or membrane breakdown that may precede necrosis (23). Ex vivo analysis of brain tumor biopsy samples has also revealed a significant positive relationship between lipids and the extent of necrosis (22). According to our experience, as well as the experience of others, lipids might indicate a high-grade tumor (Fig 2) (44, 45). Moreover, lipids have been observed in contrast-enhancing areas in patients with glioblastoma multiforme after treatment; they have been attributed to radiation necrosis (6). Nevertheless, lipids may be present in viable tumor, presumably because of poor perfusion (45) and hypoxia (46), and they undergo major intensity changes during apoptosis (47). Thus, lipids may indicate still-viable tumor that tends to become necrotic, necrotic tumor, or radiation necrosis. Presumably, low-grade gliomas do not have prominent lipid signals (Fig 3).

Because the presence of lipids is consistent with necrosis or apoptosis (22, 47), we believe that the

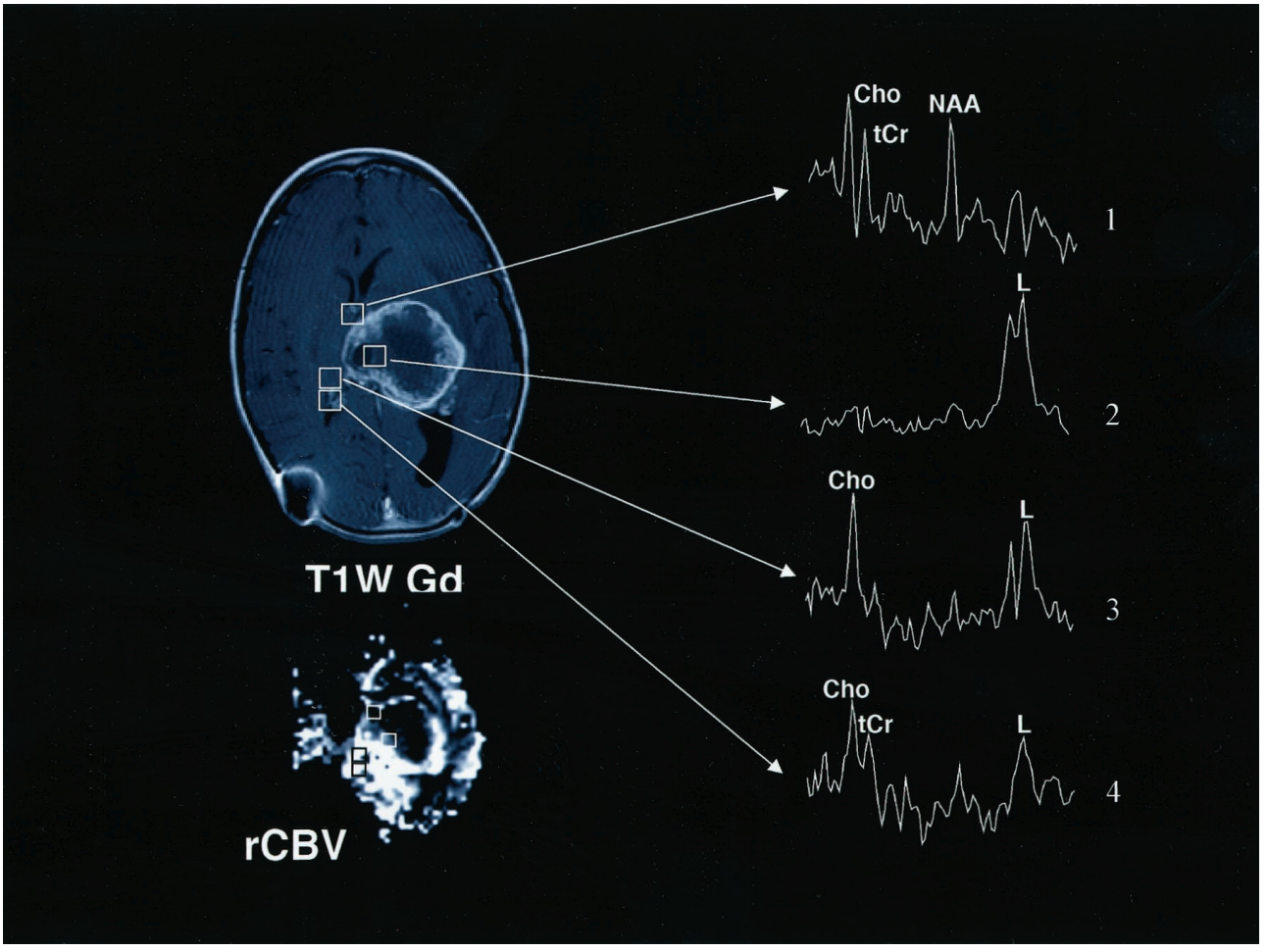

FIG 6. Images obtained at the second follow-up evaluation (1 month later) in the patient in Figure 5 include conventional axial T1-weighted Gd-enhanced (*T1W Gd*) and hemodynamic (rCBV) MR images and multivoxel MR spectroscopic data. The increased size of the mass and mass effect implied tumor progression (Fig 5). Note that regions with high Cho levels that did not enhance in Figure 5 (spectra *6* and *7*) are now enhancing. Neuropathologic analysis of stereotactic biopsy samples obtained from these regions confirmed the presence of tumor. Spectra *1–4* illustrate that hypointense regions of tumor corresponding mostly to normal tissue (spectrum *1*) and central necrosis (spectrum *2*). The high rCBV level corresponds to the ring of enhancement and regions of high Cho levels that are detected beyond the contrast-enhancing region (spectra *3* and *4*). The complementary value of multivoxel MR spectroscopic imaging and hemodynamic MR imaging is illustrated.

detection of lipids with MR spectroscopic imaging contributes independent additional information to that obtained with MR imaging. This information may improve the diagnostic accuracy of MR imaging in the differentiation of low- and high-grade tumors.

The concept that necrotic regions in tumors are hypointense on T1-weighted images (as seen in the posterior aspect of the tumor in Fig 4, which is dominated by prominent lipids and less prominent Cho signals) is also plausible. Whether necrotic tissue enhances with Gd-DTPA has been a topic of debate (13, 14).

Tumor MR Spectral Patterns

In our study, the different MR spectral patterns suggested that MR spectroscopic imaging can be used to distinguish at least three different tissue compartments—normal, tumor, and necrosis—whereas mixed MR spectral patterns were due to the known heterogeneity of tumors, as confirmed by the histopathologic features (Figs 2–6). These observations were in agreement with those of previous reports (5, 6, 44). MR spectral patterns with elevated Cho and lipid levels in the absence of NAA that were histologically verified to represent regions of active tumor with extensive areas of necrosis suggested that such MR spectral patterns contribute additional information that is not available with conventional MR imaging. Because glial tumors are graded according to their cellularity, proliferative activity, and degree of necrosis, Cho mapping (increased cellularity and proliferative activity), may added value to MR neuroimaging in patients with brain tumors, especially when it is combined with lipid mapping (necrosis and/or apoptosis). Indeed, contrast-enhancing regions with high lipid levels and low or no Cho levels, as shown in 11 patients with malignant or inoperable tumors, have been suggested to represent areas of high neoplastic potential intermingled with microscopic necrosis; this finding was verified at biopsy in four patients.

Gd-DTPA Enhancement and Hemodynamic and Diffusion-Weighted MR Imaging

Gd-DTPA enhancement on conventional MR images was not correlated with the rCBV (Fig 1C), and rCBV and ADC maps did not show abnormal rCBV or ADC values outside the Gd-DTPA–enhanced tumor bed (Fig 2), except during the follow-up examination of patients with progressing tumors (Fig 6). These findings were consistent with the notion that Gd-DTPA enhancement occurs in areas of blood-brain barrier breakdown and that it coincides with bright regions on hemodynamic images (Figs 2, 4). They also indicate that abnormal hemodynamics are correlated with active tumor, as previous investigators have suggested (21, 48). Others have also confirmed, histologically and angiographically, that hemodynamic images are associated with tumor vascularization (49). Nevertheless, according to other groups, maps of the rCBV cannot be used to differentiate between viable tumor and adjacent gray matter, and they cannot be used to reliably assess tumor progression (6).

In our study, varying degrees of Gd-DTPA enhancement on conventional brain tumor MR images were probably due to increased permeability of microvessels, a feature of neovascularity in human neuroglial tumors (50). This variability in enhancement limits the capability of conventional MR imaging in discriminating among types of tumors and between residual or recurrent tumor and postsurgical changes or radiation necrosis. In certain situations, it may prevent the generation of hemodynamic images, which are based on dynamic susceptibility contrast-enhanced imaging; this, in turn, is based on the assumption that the contrast agent remains within the intravascular space. This factor may complicate the results on postsurgical images or those in cases of radiation necrosis. In both situations, permeable vasculature may be present, and enhancement may or may not occur. In addition, controversial results have been reported in necrotic tumors, which may (51, 52) or may not (53, 54) enhance. Nevertheless, central necrotic regions surrounded by layers of ischemic tissue with a stabilized microcirculation and an advancing front with angiogenesis have been recognized in experimental cancers (50). This result is in agreement with our observations of more pronounced hemodynamics in the outer nonnecrotic regions of tumors, which are presumed to coincide with the advancing front of angiogenesis (Fig 2).

Our study revealed a negative correlation between Gd-DTPA enhancement and ADC and illustrated that Gd-DTPA enhancement (which typically occurs in areas of blood-brain barrier breakdown) coincides with hypointense regions on ADC images (Fig 2). However, ADC maps did not show abnormal ADC values outside the Gd-DTPA–enhanced tumor bed, as illustrated in Figure 2. This finding does not minimize the value of ADC maps, especially for monitoring pediatric brain tumors. This use was not assessed in the present study, but it has been suggested in a growing body of literature about the role of diffusion-weighted imaging of cerebral tumors (55) and by the notion that the ADC characterizes the biophysical characteristics of tissue microstructrure and microdynamics (55–57) and that it provides information (based on pathophysiologic characteristics) that differs from that obtained with contrast-enhancing imaging (58). In support of the above notion, Sugahara et al (59) reported that the minimum ADC value of high-grade gliomas is significantly higher than that of low-grade gliomas and that low ADC values were found in areas of increased cellularity. Others have suggested that the ADC may assist in the early detection of responses to anticancer therapy, because an increase in ADC values has been noted after treatment; this finding is consistent with an increase in the fraction of interstitial water due to treatment-induced cell death (60).

Finally, the analysis of the data in this study did not permit determination of whether rCBV and ADC mapping contribute independent nonrepetitive information beyond that obtained with MR imaging. Further analysis of findings from ongoing studies will reveal whether rCBV and ADC mapping can contribute to the diagnosis, grading, and monitoring of pediatric brain tumors.

Clinically Important Implications

In this study, Cho was detected outside the Gd-DTPA–enhanced tumor bed before treatment in all patients with malignant tumors. After treatment (in four patients with follow-up images) both high Cho and high rCBV values were detected outside the Gd-DTPA–enhanced tumor bed. Before treatment, these areas presumably represented areas of tumor extent. Persistence of high Cho and rCBV values in a tumor area after treatment may signify residual or recurring tumor; this information may lead to additional or alternative therapy. Lipids signify necrosis or apoptosis and, in combination with Cho, rCBV, and ADC values, add information for tumor typing. In patients with benign tumors, high Cho levels, and no lipids were present in nonenhancing areas of the tumor. Given the limited accuracy with Gd-DTPA, which is routinely used to define tumors at diagnosis and to differentiate tumor from necrosis or edema at post-treatment follow-up, the supplemental information obtained with MR spectroscopic, hemodynamic, and diffusion imaging may improve diagnostic accuracy.

Conclusion

We have shown that Gd-DTPA enhancement from conventional MR imaging is correlated with hemodynamic and diffusion measurements, but it is not correlated with MR spectroscopic parameters. MR spectroscopic imaging improves neuroimaging of pediatric brain tumors, because it enables biochemical assessment of tumor dynamics and because it depicts residual or recurrent tumor outside the Gd-DTPA–enhanced tumor bed. Hemodynamic and diffusion

imaging complements MR spectroscopic imaging. Because MR spectroscopic imaging provides additional independent information, compared with conventional MR imaging, it may prove useful in improving the accuracy of these imaging modalities.

References

1. Fitz C. **Magnetic resonance imaging of pediatric brain tumors.** *Top Magn Reson Imaging* 1993;5:174–189
2. Watanabe M, Tanaka R, Takeda N. **Magnetic resonance imaging and histopathology of cerebral gliomas.** *Neuroradiology* 1992;34: 463–469
3. Nelson SC, Friedman HS, Hockenberger B, et al. **False-positive MRI detection of recurrent or metastatic pediatric infratentorial tumors.** *Med Pediatr Oncol* 1993;21:350–355
4. Ashdown BC, Boyko OB, Uglietta JP, et al. **Postradiation cerebellar necrosis mimicking tumor: MR appearance.** *J Comput Assist Tomogr* 1993;17:124–126
5. Tzika AA, Vajapeyam S, Barnes PD. **Multivoxel proton MR spectroscopy and hemodynamic MR imaging of childhood brain tumors: preliminary observations.** *AJNR Am J Neuroradiol* 1997;18: 203–218
6. Wald LL, Nelson SJ, Day MR, et al. **Serial proton magnetic resonance spectroscopy imaging of glioblastoma multiforme after brachytherapy.** *J Neurosurg* 1997;87:525–534
7. Kleihues P, Cavenee WK. **WHO classification of tumors: pathology and genetics.** Lyon, France: IARC; 2000;314
8. Burger P, Scheithauser B. *Atlas of tumor pathology: tumors of the central nervous system.* Washington, DC: Armed Forces Institute of Pathology; 1994
9. Catalaa I, Henry R, Hanna M, Graves T, Nelson S, Vigneron D. **Three-dimensional diffusion, perfusion and H1-spectroscopy measures in glioma.** In: *Proceedings of the International Society For Magnetic Resonance In Medicine 2000.* Denver, Co: International Society For Magnetic Resonance In Medicine; 2000;1114
10. Robertson RL, Maier SE, Robson CD, Mulkern RV, Karas PM, Barnes PD. **MR line scan diffusion imaging of the brain in children.** *AJNR Am J Neuroradiol* 1999;20:419–425
11. Preul MC, Caramanos Z, Collins DL, et al. **Accurate, noninvasive diagnosis of human brain tumors by using proton magnetic resonance spectroscopy.** *Nat Med* 1996;2:323–325
12. Zar J. *Biostatistical Analysis.* 3rd ed. Upper Saddle River, NJ; Prentice Hall; 1996
13. Sijens PE, van Dijk P, Oudkerk M. **Correlation between choline level and Gd-DTPA enhancement in patients with brain metastases of mammary carcinoma.** *Magn Reson Med* 1994;32:549–555
14. Sijens PE, Vecht CJ, Levendag PC, van Dijk P, Oudkerk M. **Hydrogen magnetic resonance spectroscopy follow-up after radiation therapy of human brain cancer: unexpected inverse correlation between the changes in tumor choline level and post-gadolinium magnetic resonance imaging contrast.** *Invest Radiol* 1995;30:738–744
15. Tedeschi G, Lundbom N, Raman R, et al. **Increased choline signal coinciding with malignant degeneration of cerebral gliomas: a serial proton magnetic resonance spectroscopy imaging study.** *J Neurosurg* 1997;87:516–524
16. Tzika AA, Vigneron DB, Ball WS Jr, Dunn RS, Kirks DR**. Localized proton MR spectroscopy of the brain in children.** *J Magn Reson Imaging* 1993;3:719–729
17. Tzika AA, Vigneron DB, Dunn RS, Nelson SJ, Ball WS Jr. **Intracranial tumors in children: small single-voxel proton MR spectroscopy using short- and long-echo sequences.** *Neuroradiology* 1996; 38:254–263
18. Byrd SE, Tomita T, Palka PS, Darling CF, Norfray JP, Fan J. **Magnetic resonance spectroscopy (MRS) in the evaluation of pediatric brain tumors, I: introduction to MRS.** *J Natl Med Assoc* 1996;88:649–654
19. Barker P, Breiter S, Soher B, et al. **Quantitative proton spectroscopy of canine brain: in vivo and in vitro correlations.** *Magn Reson Med* 1994;32:157–163
20. Miller BL, Chang L, Booth R, et al. **In vivo 1H MRS choline: correlation with in vitro chemistry/histology.** *Life Sci* 1996;58: 1929–1935
21. Knopp EA, Cha S, Johnson G, et al. **Glial neoplasms: dynamic contrast-enhanced T2*-weighted MR imaging.** *Radiology* 1999;211: 791–798
22. Cheng L, Anthony D, Comite A, Black P, Tzika A, Gonzalez R. **Quantification of microheterogeneity in glioblastoma multiforme with ex vivo high-resolution magic-angle spinning (HRMAS) proton magnetic resonance spectroscopy.** *Neurooncology* 2000;2:87–95
23. Negendank WG, Sauter R, Brown TR, et al. **Proton magnetic resonance spectroscopy in patients with glial tumors: a multicenter study.** *J Neurosurg* 1996;84:449–458
24. Shimizu H, Kumabe T, Shirane R, Yoshimoto T. **Correlation between choline level measured by proton MR spectroscopy and Ki-67 labeling index in gliomas.** *Am J Neuroradiol* 2000;21:659–665
25. Sutton L, Wang Z, Gusnard D, et al. **Proton magnetic resonance spectroscopy of pediatric brain tumors.** *Neurosurgery* 1992;31:195–202
26. Heesters MA, Kamman RL, Mooyaart EL, Go KG. **Localized proton spectroscopy of inoperable brain gliomas: response to radiation therapy.** *J Neurooncol* 1993;17:27–35
27. Szigety SK, Allen PS, Huyser-Wierenga D, Urtasun RC. **The effect of radiation on normal human CNS as detected by NMR spectroscopy.** *Int J Radiat Oncol Biol Phys* 1993;25:695–701
28. Kizu O, Naruse S, Furuya S, et al. **Application of proton chemical shift imaging in monitoring of gamma knife radiosurgery on brain tumors.** *Magn Reson Imaging* 1998;16:197–204
29. Richards T, Budinger TF. **NMR imaging and spectroscopy of the mammalian central nervous system after heavy ion radiation.** *Radiat Res* 1988;113:79–101
30. Koutcher JA, Okunieff P, Neuringer L, Suit H, Brady T. **Size dependent changes in tumor phosphate metabolism after radiation therapy as detected by 31P NMR spectroscopy.** *Int J Radiat Oncol Biol Phys* 1987;13:1851–1855
31. Burger PC, Mahley MS Jr, Dudka L, Vogel FS. **The morphologic effects of radiation administered therapeutically for intracranial gliomas: a postmortem study of 25 cases.** *Cancer* 1979;44:1256–1272
32. Duyn JH, Frank JA, Moonen CT. **Incorporation of lactate measurement in multi-spin-echo proton spectroscopic imaging.** *Magn Reson Med* 1995;33:101–107
33. Thomas MA, Ryner LN, Mehta MP, Turski PA, Sorenson JA. **Localized 2D J-resolved 1H MR spectroscopy of human brain tumors in vivo.** *J Magn Reson Imaging* 1996;6:453–459
34. Yoshino E, Ohmori Y, Imahori Y, et al. **Irradiation effects on the metabolism of metastatic brain tumors: analysis by positron emission tomography and 1H-magnetic resonance spectroscopy.** *Stereotact Funct Neurosurg* 1996;66:240–259
35. Barker PB, Glickson JD, Bryan RN. **In vivo magnetic resonance spectroscopy of human brain tumors.** *Top Magn Reson Imaging* 1993;5:32–45
36. Henriksen O. **In vivo quantitation of metabolite concentrations in the brain by means of proton MRS.** *NMR Biomed* 1995;8:139–148
37. Sijens PE, Levendag PC, Vecht CJ, van Dijk P, Oudkerk M. **1H MR spectroscopy detection of lipids and lactate in metastatic brain tumors.** *NMR Biomed* 1996;9:65–71
38. Slosman DO, Lazeyras F. **Metabolic imaging in the diagnosis of brain tumors.** *Curr Opin Neurol* 1996;9:429–435
39. Tien RD, Lai PH, Smith JS, Lazeyras F. **Single-voxel proton brain spectroscopy exam (PROBE/SV) in patients with primary brain tumors.** *AJR Am J Roentgenol* 1996;167:201–209
40. Furuya S, Naruse S, Ide M, et al. **Evaluation of metabolic heterogeneity in brain tumors using 1H-chemical shift imaging method.** *NMR Biomed* 1997;10:25–30
41. Norfray JF, Tomita T, Byrd SE, Ross BD, Berger PA, Miller RS. **Clinical impact of MR spectroscopy when MR imaging is indeterminate for pediatric brain tumors.** *AJR Am J Roentgenol* 1999;173: 119–125
42. Gaa J, Warach S, Wen P, Thangaraj V, Wielopolski P, Edelman RR. **Noninvasive perfusion imaging of human brain tumors with EPISTAR.** *Eur Radiol* 1996;6:518–522
43. Tzika AA, Zurakowski D, Poussaint TY, et al. **Proton magnetic spectroscopic imaging of the child's brain: the response of tumors to treatment.** *Neuroradiology* 2001;43:169–177
44. Ott D, Hennig J, Ernst T. **Human brain tumors: assessment with in vivo proton MR spectroscopy.** *Radiology* 1993;186:745–752
45. Kuesel AC, Donnelly SM, Halliday W, Sutherland GR, Smith IC. **Mobile lipids and metabolic heterogeneity of brain tumours as detectable by ex vivo 1H MR spectroscopy.** *NMR Biomed* 1994;7: 172–180
46. Freitas I, Pontiggia P, Barni S, et al. **Histochemical probes for the detection of hypoxic tumour cells.** *Anticancer Res* 1990;10:613–622
47. Hakumaki JM, Poptani H, Sandmair AM, Yla-Herttuala S, Kauppinen RA. **1H MRS detects polyunsaturated fatty acid accumula-**

tion during gene therapy of glioma: implications for the in vivo detection of apoptosis. *Nat Med* 1999;5:1323–1327
48. Aronen HJ, Gazit IE, Louis DN, et al. **Cerebral blood volume maps of gliomas: comparison with tumor grade and histologic findings.** *Radiology* 1994;191:41–51
49. Sugahara T, Korogi Y, Kochi M, et al. **Correlation of MR imaging-determined cerebral blood volume maps with histologic and angiographic determination of vascularity of gliomas.** *AJR Am J Roentgenol* 1998;171:1479–1486
50. Negendank WG, Brown TR, Evelhoch JL, et al. **Proceedings of a National Cancer Institute workshop: MR spectroscopy and tumor cell biology.** *Radiology* 1992;185:875–883
51. Brasch RC, Weinmann HJ, Wesbey GE. **Contrast-enhanced NMR imaging: animal studies using gadolinium-DTPA complex.** *AJR Am J Roentgenol* 1984;142:625–630
52. Cohen BH, Bury E, Packer RJ, Sutton LN, Bilaniuk LT, Zimmerman RA. **Gadolinium-DTPA-enhanced magnetic resonance imaging in childhood brain tumors.** *Neurology* 1989;39:1178–1183
53. Healy ME, Hesselink JR, Press GA, Middleton MS. **Increased detection of intracranial metastases with intravenous Gd-DTPA.** *Radiology* 1987;165:619–624
54. Brix G, Semmler W, Port R, Schad LR, Layer G, Lorenz WJ. **Pharmacokinetic parameters in CNS Gd-DTPA enhanced MR imaging.** *J Comput Assist Tomogr* 1991;15:621–628
55. Rowley HA, Grant PE, Roberts TP. **Diffusion MR imaging: theory and applications.** *Neuroimaging Clin North Am* 1999;9:343–361
56. Luby-Phelps K. **Cytoarchitecture and physical properties of cytoplasm: volume, viscosity, diffusion, intracellular surface area.** *Int Rev Cytol* 2000;192:189–221
57. Basser PJ, Pierpaoli C. **Microstructural and physiological features of tissues elucidated by quantitative-diffusion-tensor MRI.** *J Magn Reson B* 1996;111:209–219
58. Tsuchiya K, Hachiya J, Maehara T. **Diffusion-weighted MR imaging in multiple sclerosis: comparison with contrast-enhanced study.** *Eur J Radiol* 1999;31:165–169
59. Sugahara T, Korogi Y, Kochi M, et al. **Usefulness of diffusion-weighted MRI with echo-planar technique in the evaluation of cellularity in gliomas.** *J Magn Reson Imaging* 1999;9:53–60
60. Zhao M, Pipe JG, Bonnett J, Evelhoch JL. **Early detection of treatment response by diffusion-weighted 1H-NMR spectroscopy in a murine tumour in vivo.** *Br J Cancer* 1996;73:61–64